# Realization of holonomic single-qubit operations

K. Toyoda, K. Uchida, A. Noguchi, S. Haze, and S. Urabe

*Graduate School of Engineering Science, Osaka University, 1-3 Machikaneyama, Toyonaka, Osaka, Japan*

(Dated: April 24, 2013)

Universal single-qubit operations based on purely geometric phase factors in adiabatic processes are demonstrated by utilizing a four-level system in a trapped single $^{40}$Ca$^+$ ion connected by three oscillating fields. Robustness against parameter variations is studied. The scheme demonstrated here can be employed as a building block for large-scale holonomic quantum computations, which may be useful for large qubit systems with statistical variations in system parameters.

PACS numbers: 03.67.Lx, 03.67.Pp, 37.10.Ty

## I. INTRODUCTION

Experimental studies of quantum information processing (QIP) has progressed much in recent years. In studies of QIP using trapped ions, realization of small scale computation and entanglement generation with relatively high fidelity has been reported [1], which reveals that there is no fundamental obstacle to scaling a large number of ions. The upcoming challenges are large-scale operations and high-fidelity gate operations toward fault-tolerant quantum computation.

As a way to realize high-fidelity gate operations, quantum gates and quantum computation using geometric phase factors have recently been studied. This originates from Holonomic Quantum Computation (HQC) proposed by Zanardi *et al.*[2] In HQC, degenerate multiple quantum states are utilized and unitary operations are performed by varying the system Hamiltonian along a closed path in the parameter space. The final state in the HQC is dependent only on the global property of the closed path; therefore, HQC is considered to be robust against certain types of errors. Even when diabatic evolutions of the system or nondegenerate quantum states are used, similar advantages can be expected as long as the unitary operations performed are determined by geometric phase factors [Geometric Quantum Computation (GQC)[3]].

There have been a number of experiments in different systems related to GQC [4–8]. It is known that universal quantum computation can be realized with a combination of single-qubit and two-qubit operations [9]. As demonstrations of two qubit operations in trapped-ion systems, "Geometric-phase gate" by Leibried *et al.* [5] and the Mølmer-Sørensen gate [8, 10, 11] have been realized. A gate fidelity of 99.3% has been realized using such a scheme [8].

Single qubit operations in trapped-ion systems have been performed to date using a dynamical method with variable pulse lengths and phases. By replacing such a method with those that use geometric phases, gate operations that are robust against variation of parameters such as pulse intensity and lengths can be expected.

In this work, we report the realization of purely geometric single qubit operations using a four-level system in a single $^{40}$Ca$^+$ ion. Three transitions in the four-level system are excited either by three optical fields or by two optical fields and one RF magnetic field. Rotation operations by arbitrary angles along two different axes, $X$ and $Z$ in the Bloch sphere for the qubit, are demonstrated by utilizing stimulated Raman adiabatic passage (STIRAP) in this four-level system. Robustness against parameter variations is also demonstrated.

This work is based on proposals using a *tripod* system comprising of one upper state and three lower states connected by three oscillating fields [12–15]. There are two dark states in the system, and those dark states are adiabatically manipulated with the intensities and phases of the oscillating fields to perform single-qubit operations.

There was also a proposal and demonstrations of single-qubit operations using geometric phase factors using a two-level system and square pulses [6, 7]. However, to the best of our knowledge no adiabatic (or holonomic) demonstration of single-qubit operations using dark states has been reported so far.

## II. PRINCIPLES FOR HOLONOMIC SINGLE-QUBIT OPERATIONS

Here the formalization of the scheme is summarized based on Kis and Renzoni [13] for later reference. A four-level system comprising of $\{|0\rangle, |1\rangle, |2\rangle, |u\rangle\}$ is considered [see Fig. 1(a)]. $|0\rangle$ and $|1\rangle$ span a qubit manifold, while $|u\rangle$ represents an upper state and $|2\rangle$ represents an auxiliary state used in STIRAP. Three near resonant oscillating fields are applied to this system between $|u\rangle$ and $|k\rangle$ $(k = 0, 1, 2)$, and the Hamiltonian in the interaction picture with the rotating wave approximation is given as

$$H(t) = -\hbar\delta |u\rangle \langle u| + \frac{\hbar}{2} \sum_{k=0}^{2} [\Omega_k(t) |u\rangle \langle k| + \text{H.c.}], \quad (1)$$

where $\delta$ is the detuning of the lasers, which is assumed to be common to all the three transitions. The Rabi frequencies for the transitions between $|u\rangle$ and the qubit states are $\Omega_0(t) \equiv \Omega(t)\cos\theta_1$ (assumed to be real) and $\Omega_1(t) \equiv \Omega(t)e^{i\phi_1}\sin\theta_1$, where a real quantity $\Omega(t)$ is the common envelope function. $\theta_1 = \tan^{-1}|\Omega_1(t)/\Omega_0(t)|$ and $\phi_1 = \arg\Omega_1(t)$ are assumed to be independent of time.

The Rabi frequency between $|u\rangle$ and $|2\rangle$ is described as $\Omega_2(t) \equiv |\Omega_2(t)|e^{i\phi_2(t)}$ with $\phi_2(t) = \arg \Omega_2(t)$.

The following states in the qubit manifold are useful for describing the Hamiltonian and explaining the gate procedure: $|C_1\rangle = \cos\theta_1 |0\rangle + e^{-i\phi_1} \sin\theta_1 |1\rangle$ and $|D_1\rangle = -\sin\theta_1 |0\rangle + e^{-i\phi_1} \cos\theta_1 |1\rangle$, and similarly, the following states in the total lower-state manifold spanned by $\{|0\rangle, |1\rangle, |2\rangle\}$: $|C_2\rangle = \cos\theta_2(t) |C_1\rangle + e^{-i\phi_2(t)} \sin\theta_2(t) |2\rangle$ and $|D_2\rangle = -\sin\theta_2(t) |C_1\rangle + e^{-i\phi_2(t)} \cos\theta_2(t) |2\rangle$, where $\theta_2(t) = \tan^{-1} |\Omega_2(t)/\Omega(t)|$. Based on these, the Hamiltonian can be simplified as follows:

$$H(t) = -\hbar\delta |u\rangle\langle u| + \frac{\hbar}{2}\Omega_{\text{total}}(t)\left(|u\rangle\langle C_2| + \text{H.c.}\right), \quad (2)$$

where $\Omega_{\text{total}}(t) \equiv \left[\Omega^2(t) + |\Omega_2(t)|^2\right]^{1/2}$. When $\delta = 0$, this Hamiltonian has four eigenvectors $\{|D_1\rangle, |D_2\rangle, |B_+\rangle, |B_-\rangle\}$ with eigenvalues of $\{0, 0, \hbar\Omega_{\text{total}}(t)/2, -\hbar\Omega_{\text{total}}(t)/2\}$, respectively, where $|B_\pm\rangle = (|C_2\rangle \pm |u\rangle)/\sqrt{2}$.

We proof the ability to perform arbitrary single-qubit operations by first starting from an arbitrary initial state in the qubit manifold, $|\psi_0\rangle \equiv \alpha |0\rangle + \beta |1\rangle$, which can be rewritten using $|C_1\rangle$ and $|D_1\rangle$ as $|\psi_0\rangle = \langle C_1|\psi_0\rangle |C_1\rangle + \langle D_1|\psi_0\rangle |D_1\rangle$. This initial state will be transferred in the first STIRAP sequence that makes use of $|D_2\rangle$ [the left half in Fig. 1(b), with $\theta_2(t) : \pi/2 \to 0$ and $\phi_2 = \arg\Omega_2 = 0$] to the intermediate state $|\psi_1\rangle = -\langle C_1|\psi_0\rangle |2\rangle + \langle D_1|\psi_0\rangle |D_1\rangle$. This intermediate state will then be transferred using the second STIRAP sequence [the right half in Fig. 1(b), with $\theta_2(t) : 0 \to \pi/2$ and $\phi_2 = \arg\Omega_2 = \Phi$] to the final state $|\psi_2\rangle = e^{i\Phi}\langle C_1|\psi_0\rangle |C_1\rangle + \langle D_1|\psi_0\rangle |D_1\rangle$, which can be rewritten using the identity operator $\hat{I}$ and the Pauli operators $\hat{\sigma} = (\hat{\sigma}_x, \hat{\sigma}_y, \hat{\sigma}_z)$ on the computational manifold $\{|0\rangle, |1\rangle\}$ as $|\psi_2\rangle = e^{i\Phi/2}[\cos(\Phi/2)\hat{I} + i\mathbf{n}\cdot\hat{\sigma}\sin(\Phi/2)]|\psi_0\rangle$ with $\mathbf{n} = (\sin 2\theta_1 \cos\phi_1, -\sin 2\theta_1 \sin\phi_1, \cos 2\theta_1)$. This operation corresponds to a rotation by angle $-\Phi$ around $\mathbf{n}$, which can be taken arbitrarily by selecting the values for $\theta_1$ and $\phi_1$, hence arbitrary single-qubit operations can be performed.

This scheme is based on adiabatic population transfer using $|D_2\rangle$, and diabatic transitions from this state to $|B_\pm\rangle$ are among the possible causes of infidelity in gate operations. The probability for such diabatic transitions is calculated to be in the order of $\max\left[2\dot{\theta}_2(t)^2/\Omega_{\text{total}}^2\right]$ [16], which should be set to be much smaller than 1 to maintain high fidelity.

## III. EXPERIMENTAL SETUP AND PROCEDURES

The experimental setup has been previously described [17] and only a brief description is given here. A single $^{40}\text{Ca}^+$ is trapped in vacuum ($6 \times 10^{-9}$ Pa) using a linear Paul trap. The trap used here is a conventional linear trap with an operating frequency of 23 MHz and secular frequencies of $(\omega_x, \omega_y, \omega_z)/2\pi = (2.4, 2.2, 0.69)$ MHz. A bias magnetic field of $2.9 \times 10^{-4}$ T is applied to define a quantization axis, which results in a Zeeman splitting of $\sim$4.9 MHz between $D_{5/2}$ sublevels. In experiments that employ three optical fields, a titanium sapphire laser at 729 nm stabilized to a high-finesse low-thermal-expansion cavity is used for the excitation of ions between $S_{1/2}$ and $D_{5/2}$. The amplitudes and frequencies of the three optical fields at 729 nm are changed by varying the three RF fields that are combined and fed to an acousto-optic modulator. The RF fields are generated by three direct-digital synthesis (DDS) boards that are controlled by a field-programmable gate array. Polarization of the optical fields is adjusted so that there are polarizations both parallel and perpendicular to the bias magnetic field; therefore, the transition to be excited is selected by changing the frequencies of the DDS boards. In experiments that employ two optical fields and one RF magnetic field, an RF coil in the vicinity of the trap is used to generate the RF field. The details of the RF excitation procedure are similar to that described in Ref. [18].

We have chosen the $S_{1/2}$–$D_{5/2}$ electric-quadrupole transition of $^{40}\text{Ca}^+$ for realizing the geometric phase gate. The encoding of the tripod system to the sublevels in $S_{1/2}$ and $D_{5/2}$ is as follows: $S_{1/2}(m_j = -1/2)$ as the "upper" state $|u\rangle$ and three Zeeman sublevels in $D_{5/2}$ ($m_j = -3/2, 1/2, -5/2$) as the lower states $|0\rangle$, $|1\rangle$ and $|2\rangle$, respectively (see Fig. 1(c)). The reason that a level in $S_{1/2}$ is adopted instead of one in $P_{3/2}$ as $|u\rangle$ is to avoid the effects of spontaneous emissions when all the fields are resonant. However, unwanted couplings between $S_{1/2}(m_j = 1/2)$ and $|0\rangle$, $|1\rangle$ and $|2\rangle$ must still be considered. Since these couplings are off resonance, varying $\theta_2(t)$ leads to time-dependent AC-Stark shifts that disturb the null eigenenergies of the qubit states. This effect was numerically evaluated with realistic parameters and the phase accumulated during the gate operation was confirmed to be smaller than 0.5 rad under typical experimental conditions in the present work.

We essentially do not compensate such AC-Stark shifts for the present work. In the experiments in §IV and of rotations by angle $\pi$ in §V, we adjust one of the detunings (one for $|u\rangle$–$|0\rangle$) so that fringe shift resulting from AC-Stark shifts are apparently canceled. This cancelation depends on the details of the STIRAP pulses, including such conditions as peak Rabi frequencies, pulse shapes or total time (it may not depend on such conditions as input states or rotation angles since AC Stark shifts do not depend on these). We also evaluate gate performances without cancellation of this type by examining rotations by angle $\pi/2$ with relatively low Rabi frequencies in §V and §VIII.

The procedure for gate operations is as follows. Firstly, the ion is cooled to near the motional ground state with Doppler cooling by 397 and 866 nm and with sideband cooling of the axial motion by lasers at 729 and 854 nm. The average motional quantum number along axial direc-

tion after sideband cooling is $\bar{n}_z = 0.06$. Optical pumping using a 397 nm $\sigma^-$ transition is then performed to initialize the ion in $S_{1/2}(m_j = -1/2)$ ($|u\rangle$). The ion is transferred from $|u\rangle$ to the computational manifold spanned by $\{|0\rangle, |1\rangle\}$ using square $\pi$ pulses, and then a gate STIRAP pulse sequence is applied between $|0\rangle$ and $|1\rangle$. The pulse shape of the gate consists of partially overlapping sinusoidal curves and constant values, as in Fig. 1(d). A step variation of $\phi_2(t)$ by $\Phi$, which brings a geometric phase factor, is given at the middle of the gate sequence where $|\Omega_2(t)| = 0$. After the gate sequence, a square $\pi$ pulse is applied to map the state of $|0\rangle$ to $|u\rangle$. An additional pulse may also be applied, depending on the element of the density matrix to be observed. State discrimination is performed by detecting fluorescence from the ion with a photomultiplier tube during a period of 7 ms when 397 and 866 nm fields are applied[19].

The time dependence of the optical pulses is chosen as follows ($t_1 = 0$, $t_1 = (1 - \alpha)T$, $t_2 = T$ and $t_3 = (2 - \alpha)T$ where $0 \leq \alpha \leq 1$):

$$\Omega^2(t) = \begin{cases} 0 & (t < t_0) \\ \Omega_{\max}^2(1 - \cos^2 \pi t/2T) & (t_0 \leq t < t_2) \\ \Omega_{\max}^2 & (t_2 \leq t < t_3) \\ 0 & (t \geq t_3), \end{cases} \quad (3)$$

$$|\Omega_2(t)|^2 = \begin{cases} 0 & (t < t_0) \\ \Omega_{2,\max}^2 & (t_0 \leq t < t_1) \\ \Omega_{2,\max}^2 \cos^2 \pi(t - t_1)/2T & (t_1 \leq t < t_3) \\ 0 & (t \geq t_3), \end{cases} \quad (4)$$

where $\Omega_{\max}^2$ and $\Omega_{2,\max}^2$ are the maximum values for $\Omega^2(t)$ and $|\Omega_2(t)|^2$, respectively. In the experimental results given in this article, the values of $\alpha$ were empirically chosen to in between 0.55 and 0.85 so that effective population transfer was attained in experiments and/or numerical simulations. It is noted that the values of $\alpha$ used in this article are not thoroughly optimized ones but those that give relatively good performances among tested.

## IV. RESULTS FOR $X$- AND $Z$-ROTATIONS

We show that arbitrary one-qubit operations can be realized with the geometric method introduced here. This can be accomplished by showing $X$- and $Z$-rotations independently, because arbitrary operations can be decomposed into sequences of such rotations.

The procedure for $X$-rotations is as follows. The ion is first prepared in $|u\rangle$ by sideband cooling and optical pumping, then initialized to $|0\rangle$, and a STIRAP sequence is applied to perform a geometric gate. After this, the populations of the final states are analyzed by mapping the qubit states to the optical transition using a rectangular $\pi$ pulse on $|i\rangle \leftrightarrow |u\rangle$ ($i = 0, 1, 2$). The populations in $|2\rangle$ and $|u\rangle$ are also measured to verify that

the gate operation is closed to the manifold spanned by the qubit states $\{|0\rangle, |1\rangle\}$. $\Omega_0$ and $\Omega_1$ are adjusted to be equivalent, and the peak values for $(\Omega_0, \Omega_1, \Omega_2)/2\pi$ are $\sim (125, 125, 170)$ kHz. The total time for the STIRAP sequence is set to be $\sim 120$ $\mu$s by taking appropriate account of the adiabaticity. $\alpha = 0.85$ is used for the results given in this section.

Figure 2(a) shows the results for $X$-rotations. A sinusoidal oscillation of population between $|0\rangle$ and $|1\rangle$ is observed. The sum of populations in the other states $|2\rangle$ and $|u\rangle$ is below 0.05 over the entire region, with which we confirm that the rotation operations are almost limited to the computational manifold spanned by $\{|0\rangle, |1\rangle\}$. The contrasts of the populations of $|0\rangle$ and $|1\rangle$ are obtained by fitting to $0.951 \pm 0.009$ and $0.975 \pm 0.008$, respectively.

The procedure for observation of $Z$-rotations is similar to Ramsey interferometry. A superposition of the qubit states $|0\rangle$ and $|1\rangle$ is first prepared by application of a $\pi/2$ pulse on $|u\rangle$–$|1\rangle$ and a $\pi$ pulse on $|u\rangle$–$|0\rangle$. A $Z$-rotation is then performed with STIRAP, which is followed by a $\pi$ pulse on $|u\rangle$–$|0\rangle$ and a $\pi/2$ pulse on $|u\rangle$–$|1\rangle$. The last pulse causes an interference between $|u\rangle$ and $|1\rangle$, which is detected by a projection measurement using fluorescence. Here the peak values for $(\Omega_0, \Omega_1, \Omega_2)/2\pi$ are set to be $\sim (200, 0, 170)$ kHz and the total time for the STIRAP sequence is $\sim 120$ $\mu$s. Figure 2(b) represents the results for $Z$-rotations, which shows a population oscillation against $\Phi$ with an almost unit contrast. From a least-squares fit, the contrast is obtained to be $0.937 \pm 0.010$.

## V. EVALUATION OF FIDELITY

In order to investigate the action of gate operations more quantitatively, we also performed estimation of gate fidelities by using quantum state tomography. We performed fidelity estimation in the following three cases: (a) X-rotation by angle $\pi$, (b) Z-rotation by angle $\pi$, and (c) Hadamard gate [rotation around $\mathbf{n} = (1/\sqrt{2}, 0, -1/\sqrt{2})$ in the Bloch sphere by angle $\pi$]. As explained before, general operations of the STIRAP gate can be described as the following unitary operator:

$$\hat{U}_{\text{STIRAP}}(\theta_1, \phi_1, \Phi)$$
$$\equiv e^{i\Phi/2} \left[ \cos \frac{\Phi}{2} \hat{I} + i\mathbf{n}(\theta_1, \phi_1) \cdot \hat{\sigma} \sin \frac{\Phi}{2} \right] \quad (5)$$

where $\mathbf{n}(\theta_1, \phi_1) \equiv (\sin 2\theta_1 \cos \phi_1, -\sin 2\theta_1 \sin \phi_1, \cos 2\theta_1)$. Using this general expression, the unitary operators for the three cases given above are respectively written as follows:

$$\hat{U}_X \equiv \hat{U}_{\text{STIRAP}}(\pi/4, 0, \pi), \quad (6)$$
$$\hat{U}_Z \equiv \hat{U}_{\text{STIRAP}}(0, 0, \pi), \quad (7)$$
$$\hat{U}_H \equiv \hat{U}_{\text{STIRAP}}(3\pi/8, 0, \pi). \quad (8)$$

The initial states in the three cases are respectively prepared as follows: (a)$|\psi_{0X}\rangle \equiv |0\rangle$, (b)$|\psi_{0Z}\rangle \equiv (-i|0\rangle +$

$|1\rangle)/\sqrt{2}$, and (c)$|\psi_{0H}\rangle \equiv |0\rangle$. In order to take into account imperfect preparation of these initial states, we performed measurement of these states using the technique of quantum state tomography. In the encoding adopted here, both the two states $|0\rangle$ and $|1\rangle$ in the computational subspace are in the same electronic state $D_{5/2}$. In order to discriminate these two states, we applied a mapping pulse between $|0\rangle$ and $|u\rangle$ before performing fluorescence detection. The population out of the computational manifold (population in $|1\rangle$ and $|u\rangle$) before application of the mapping pulse, which is typically below 0.05 as described before, is ignored here for simplicity. The mapping pulse itself produces a geometric phase relative to the other states ($|1\rangle$ and $|2\rangle$), which should be taken into account properly in the fidelity analysis. The mapping operation can be described as follows:

$$\hat{R}_{\mathrm{SWAP},0u} \equiv -i|0\rangle\langle u| - i|u\rangle\langle 0| + |1\rangle\langle 1| + |2\rangle\langle 2|. \quad (9)$$

This corresponds to a rotation by angle $\pi$ around the $x$ axis in the Bloch sphere of the two-level system $\{|0\rangle, |u\rangle\}$.

The density matrix after application of the mapping pulse were reconstructed (using linear reconstruction) by fluorescence detection and an optional $\pi/2$ pulse prior to that. The populations along three orthogonal axes in the Bloch sphere, $P_{x1i}, P_{y1i}$ and $P_{z1i}$, are measured, where $P_{x1i}$ ($P_{y1i}$) is the population in $D_{5/2}$ after the mapping pulse and a $\pi/2$ pulse with the phase $-3\pi/2$ (0) on $|u\rangle$–$|1\rangle$, and $P_{z1i}$ is the population in $D_{5/2}$ state immediately after the mapping pulse. Using the Bloch vector $\mathbf{r} = (r_x, r_y, r_z) = (1-2P_{x1i}, 1-2P_{y1i}, 1-2P_{z1i})$ the density operator after the mapping pulse is expressed as

$$\hat{\rho}_{i,obs}$$
$$\equiv \frac{1}{2}\hat{I} + \frac{r_x}{2}(|u\rangle\langle 1| + |1\rangle\langle u|) + \frac{r_y}{2}(-i|u\rangle\langle 1| + i|1\rangle\langle u|)$$
$$+ \frac{r_z}{2}(|u\rangle\langle u| - |1\rangle\langle 1|), \quad (10)$$

and by using this the initial density operator is described as follows:

$$\hat{\rho}_i \equiv \hat{R}^{\dagger}_{\mathrm{SWAP},0u}\hat{\rho}_{i,obs}\hat{R}_{\mathrm{SWAP},0u}. \quad (11)$$

In a similar way, the final density operator just after STIRAP gate operations, $\hat{\rho}_f$, is obtained in terms of populations $P_{x1f}, P_{y1f}$ and $P_{z1f}$ (defined in the same way as above) after a mapping pulse that follows the gate operation.

The gate fidelities in the three cases can be described using the density operators and the unitary operators, as follows:

$$F_X \equiv \mathrm{tr}\left(\hat{\rho}_f\hat{U}_X\hat{\rho}_i\hat{U}_X^{\dagger}\right), \quad (12)$$
$$F_Z \equiv \mathrm{tr}\left(\hat{\rho}_f\hat{U}_Z\hat{\rho}_i\hat{U}_Z^{\dagger}\right), \quad (13)$$
$$F_H \equiv \mathrm{tr}\left(\hat{\rho}_f\hat{U}_H\hat{\rho}_i\hat{U}_H^{\dagger}\right). \quad (14)$$

The fidelities are explicitly written in terms of the initial and final populations, as follows:

$$\begin{aligned} F_X &= P_{x1i} + P_{x1f} - 2P_{x1i}P_{x1f} \\ &\quad -P_{y1i} - P_{y1f} + 2P_{y1i}P_{y1f} \\ &\quad +P_{z1i} + P_{z1f} - 2P_{z1i}P_{z1f}, \quad (15) \\ F_Z &= P_{x1i} + P_{x1f} - 2P_{x1i}P_{x1f} \\ &\quad +P_{y1i} + P_{y1f} - 2P_{y1i}P_{y1f} \\ &\quad -P_{z1i} - P_{z1f} + 2P_{z1i}P_{z1f}, \quad (16) \\ F_H &= P_{x1i} + P_{x1f} - 2P_{x1i}P_{x1f} \\ &\quad +P_{y1i} + P_{z1f} + 2P_{y1i}P_{z1f} \\ &\quad +P_{z1i} + P_{y1f} - 2P_{z1i}P_{y1f} - 1. \quad (17) \end{aligned}$$

In order to determine the confidence intervals of the fidelities, we obtained variances of the fidelities considering propagation of uncertainty based on the above expression, as follows:

$$V(F_X)$$
$$= V(P_{x1i}) + V(P_{x1f}) + 4P_{x1i}^2V(P_{x1f}) + 4P_{x1f}^2V(P_{x1i})$$
$$\quad V(P_{y1i}) + V(P_{y1f}) + 4P_{y1i}^2V(P_{y1f}) + 4P_{y1f}^2V(P_{y1i})$$
$$\quad V(P_{z1i}) + V(P_{z1f}) + 4P_{z1i}^2V(P_{z1f}) + 4P_{z1f}^2V(P_{z1i}),$$
$$V(F_Z) = V(F_X),$$
$$V(F_H)$$
$$= V(P_{x1i}) + V(P_{x1f}) + 4P_{x1i}^2V(P_{x1f}) + 4P_{x1f}^2V(P_{x1i})$$
$$\quad V(P_{y1i}) + V(P_{z1f}) + 4P_{y1i}^2V(P_{z1f}) + 4P_{z1f}^2V(P_{y1i})$$
$$\quad V(P_{z1i}) + V(P_{y1f}) + 4P_{z1i}^2V(P_{y1f}) + 4P_{y1f}^2V(P_{z1i}),$$

where $V(...)$ represents the variance of each quantity. The variances of the populations [such as $V(P_{x1i})$] are simply determined here as the variances in binomial distributions; e.g. $V(P_{x1i}) = P_{x1i}(1 - P_{x1i})/N$, where $N$ is the number of experiments per one measurement condition. The confidence intervals (68%) for the fidelities are determined as the square roots of the variances of the fidelities.

Table I shows the results for the initial and final population measurements. The measurements were performed in essentially the same conditions as used in the previous section. Using the measured populations, the fidelities are estimated and shown in Table II. The second column in Table II shows the fidelities reflecting both initial and final populations. We should note that these values are largely affected by imperfect initialization and analysis and therefore should be rather taken as the lower limits for the fidelities.

For the purpose of reference, we also estimated the fidelities when ideal initial or final states are assumed (the third and fourth columns in Table II, respectively). The fidelities for ideal initial states (the third column) represent the goodness of the generated states without considering initialization errors. These values that are better than those in the second column can be considered as the upper limits for the fidelities (when all operations other than the gates are assumed to be perfect). The

| Gate type | $P_{x1i}$ | $P_{y1i}$ | $P_{z1i}$ | $P_{x1f}$ | $P_{y1f}$ | $P_{z1f}$ |
|---|---|---|---|---|---|---|
| X-$\pi$ | 0.510 | 0.549 | 0.026 | 0.463 | 0.555 | 0.985 |
| Z-$\pi$ | 0.509 | 0.045 | 0.502 | 0.472 | 0.973 | 0.499 |
| Hadamard | 0.497 | 0.515 | 0.025 | 0.485 | 0.989 | 0.488 |

TABLE I: Results of population measurements for fidelity estimation. The initial ($\{P_{x1i}, P_{y1i}, P_{z1i}\}$) and final ($\{P_{x1f}, P_{y1f}, P_{z1f}\}$) populations in the different three bases are measured for three different types of gate operations (see the text for details). Each result is obtained as the average of 1500 experiments.

| Gate type | Fidelity | Fidelity (ideal initial states) | Fidelity (ideal final states) |
|---|---|---|---|
| X-$\pi$ | 0.965±0.038 | 0.985±0.026 | 0.974±0.027 |
| Z-$\pi$ | 0.931±0.038 | 0.973±0.036 | 0.955±0.039 |
| Hadamard | 0.965±0.038 | 0.989±0.026 | 0.975±0.027 |

TABLE II: Estimated fidelities. The confidence intervals are for 68% confidence level. The second column shows fidelities calculated from the measured initial and final populations. The third and fourth columns show estimated fidelities when ideal initial or final states are assumed, respectively, for the purpose of reference (see the text for details).

fidelities for ideal final states (the fourth column) represent the goodness of the initialization process. These values support the observation that the values in the second column is largely affected by imperfect initialization (and possibly imperfect analysis).

We also performed fidelity analysis for STIRAP gates with rotation angle of $\pi/2$, which are more sensitive to coherence between STIRAP and square-pulse operations and hence to AC Stark shifts. Table III shows the results for the initial and final population measurements for X and Z gates. Either $|+x\rangle \equiv (|0\rangle + |1\rangle)/\sqrt{2}$ or $|+z\rangle \equiv |0\rangle$ as specified are used as the initial state. It should be noted that this time AC Stark shifts are not compensated at all, and relatively small values of the Rabi frequencies are used to suppress their effect. The peak values for $(\Omega_0, \Omega_1, \Omega_2)/2\pi$ are set to be $\sim(33.5, 33.7, 47.0)$ kHz for X gates and $\sim(47.3, 0, 47.2)$ kHz for Z gates. The total time for the STIRAP sequence is $\sim 290$ $\mu$s and $\alpha = 0.75$ is used. The results of population measurements are shown in Table III. Using these populations, the fidelities and their confidence intervals are estimated in the same way as above and shown in Table IV.

It should be noted that the fidelities in the case of ideal final states in Table IV are higher than what are given in Table II. When taking the results in Table III, we used a noise eater with a sample and hold capability to reduce fluctuations in the amplitudes of the square pulses. We speculate that this helped improving the operational fidelity of the initialization.

| Gate type | $P_{x1i}$ | $P_{y1i}$ | $P_{z1i}$ | $P_{x1f}$ | $P_{y1f}$ | $P_{z1f}$ |
|---|---|---|---|---|---|---|
| X-$\pi/2$($|+x\rangle$ prep.) | 0.009 | 0.505 | 0.515 | 0.029 | 0.611 | 0.622 |
| X-$\pi/2$($|+z\rangle$ prep.) | 0.526 | 0.540 | 0.006 | 0.595 | 0.916 | 0.363 |
| Z-$\pi/2$($|+x\rangle$ prep.) | 0.009 | 0.505 | 0.515 | 0.592 | 0.055 | 0.515 |
| Z-$\pi/2$($|+z\rangle$ prep.) | 0.526 | 0.540 | 0.006 | 0.546 | 0.534 | 0.041 |

TABLE III: Results of population measurements for fidelity estimation of X and Z gates with $\pi/2$ rotations. Either $|+x\rangle \equiv (|0\rangle + |1\rangle)/\sqrt{2}$ or $|+z\rangle \equiv |0\rangle$ as specified are used as the initial state. Each result is obtained as the average of 1500 experiments. Note that the same results are used as the initial populations for X and Z gates.

| Gate type | Fidelity | Fidelity (ideal initial states) | Fidelity (ideal final states) |
|---|---|---|---|
| X-$\pi/2$($|+x\rangle$ prep.) | 0.960±0.039 | 0.971±0.025 | 0.991±0.026 |
| X-$\pi/2$($|+z\rangle$ prep.) | 0.905±0.037 | 0.916±0.026 | 0.994±0.026 |
| Z-$\pi/2$($|+x\rangle$ prep.) | 0.936±0.038 | 0.945±0.026 | 0.991±0.026 |
| Z-$\pi/2$($|+z\rangle$ prep.) | 0.952±0.038 | 0.959±0.026 | 0.994±0.026 |

TABLE IV: Fidelities for gates with $\pi/2$ rotations estimated from measured populations in the previous table.

## VI. RESULTS FOR QUBIT ENCODING TO OPTICALLY SEPARATED LEVELS

We have also attempted encoding of the qubit into optically separated levels. Use of optically separated levels may be advantageous when considering a combination with optical two-qubit gate schemes [8, 10, 11] and use of less magnetic-field-sensitive transitions, such as $S_{1/2}(m_J = 1/2)$–$D_{5/2}(m_J = 1/2)$. This encoding uses an RF transition between the ground Zeeman sublevels [18]. Figure 1(e) shows the levels used for this encoding. $\{|0\rangle, |1\rangle, |2\rangle, |u\rangle\}$ are encoded into $S_{1/2}(m_J = 1/2)$, $D_{5/2}(m_J = -3/2)$, $D_{5/2}(m_J = -5/2)$ and $S_{1/2}(m_J = -1/2)$, respectively.

Fig. 2(c) shows the results for $X$-rotations with qubit encoding to optically separated levels. Blue hollow circles (red filled circles) represent the populations in $|0\rangle$ when $|0\rangle$ ($|1\rangle$) is initially prepared. The contrasts are $0.967 \pm 0.012$ and $0.916 \pm 0.014$ for the preparation of $|0\rangle$ and $|1\rangle$, respectively. Fig. 2(d) shows the result for $Z$-rotations, with a contrast of $0.886 \pm 0.022$. In these results, the peak values of $(\Omega_0, \Omega_1, \Omega_2)/2\pi$ are set to be $\sim (130, 100, 100)$ kHz and $\sim (130, 0, 100)$ kHz for $X$- and $Z$-rotations, respectively. The total time for the STIRAP sequence is approximately 128 $\mu$s.

In ideal cases of $X$-rotations, the peak values of $\Omega_0$ and $\Omega_1$ should be equal, which is not the case in the experiment described above. For a technical reason concerning the difference in the amplitude modulation of RF and optical fields, the temporal shapes of $\Omega_0$ and $\Omega_1$ are not proportional to each other in the present setup. The peak values given above are determined empirically so that

they give correct $X$-rotations. This imperfection may be avoided by simply calibrating the amplitude modulation process for either the RF or optical field so that $\Omega_0$ and $\Omega_1$ give exactly the same time dependency.

## VII. DEMONSTRATION OF ROBUSTNESS

The feature of the geometric phase gate is that it is expected to be robust against variations in the pulse area, namely the Rabi frequency and the pulse length. To study this feature, two experiments were conducted. One is the measurement of $X$-rotations with variation of the peak Rabi frequency and the illumination period. The other is the measurement of $Z$-rotations with variation of the peak Rabi frequency, while the illumination period is held constant. The ratios of the peak Rabi frequencies are held constant in each case. Both experiments are performed by measuring population oscillations as the rotation angle $\phi_2$ is varied.

The results for the former experiment is shown in Fig. 3 (a) and (b) for three values of the illumination period, with (a) fringe contrasts and (b) shifts. The ratios of the Rabi frequencies are held constant, and the peak values of $\Omega_0/2\pi$ are shown in the horizontal axes as representatives of the Rabi frequencies. $\alpha = 0.55$ was used for the results given in Fig. 3, which gave relatively high contrasts for the case of $\Omega_2/2\pi \sim 20$ kHz. There is a region (above $10\sim30$ kHz) over which the absolute values of the fringe contrasts are almost independent of the Rabi frequency, which demonstrates the robustness. The fringe shifts are expected to start from zero and increase quadratically as the Rabi frequency is increased due to the increase of AC Stark shifts. The observed shifts shown in Fig. 3 (b) basically follow this expectation.

The results for the latter experiment are shown in Fig. 3(c) and (d) with (c) fringe contrasts and (d) shifts. The fringe contrasts do not change appreciably as the peak Rabi frequency is varied in the region above 20 kHz.

We have performed numerical simulations trying to explain the loss of fringe contrasts and the shifts. Simulations are performed using a Liouville equation with decay terms representing laser-frequency and magnetic-field flucutuations. AC Stark shifts due to different Zeeman components and electric-dipole-allowed transitions ($S_{1/2}$–$P_{1/2}$, $S_{1/2}$–$P_{3/2}$ and $D_{5/2}$–$P_{3/2}$) are fully taken into account as time-dependent variation of the detunings. The results are shown as curves in Fig. 3, where overall qualitative and partial quantitative agreements between experimental and numerical results are obtained.

## VIII. DISCUSSIONS

The possible factors for loss of fidelity in the previously described results includes laser frequency and magnetic field fluctuations. The laser linewidth in the current setup is $\sim 300$ Hz and the magnetic field fluctuations corresponds to fluctuations of resonance frequencies of up to $\sim 30$ Hz. The effects of thermal distribution of motional quantum numbers and intensity fluctuations are negligible, because the scheme used here is robust against variations in Rabi frequencies.

We performed numerical simulations (similar to what is described in the previous section) to evaluate the fidelity of some of the gates given in in §V. For X-rotation by angle $\pi$ and Z-rotation by angle $\pi$, the dominant infidelity factor was the effect of magnetic field fluctuations ($\sim$1 %). Infidelity due to diabaticity was estimated to be $\sim$0.2%. The contribution from laser-frequency fluctuations in this case was below 0.1 %. This can be explained by the fact that the scheme is not sensitive to one-photon detunings but only to two-photon detunings (as will be described later in this section). The contribution from laser-frequency fluctuations may be larger when the encoding as in §VI is used. AC Stark shifts were compensated in this case by detuning one of the beams as described before. The possible fidelity loss from not performing compensation would amount to 20–30 % in our simulation.

For the results of X- and Z-rotations by angle $\pi/2$, the largest infidelity factor was diabaticity (2–5 %), and the effect of magnetic field fluctuations was 1–3 %. Although no AC-Stark-shifts compensation was performed in this case, infidelity due to AC Stark shifts was as small as 0–1 %, and the effect of laser-frequency fluctuations was 0.2–0.3 %.

The scheme demonstrated here is useful not only for atomic systems (neutral or ionic), but also for other systems including solid-state systems. The scheme is effective for those systems where the coherence time is relatively long, but inhomogeneities of the excitation field intensities cannot be avoided, or for those where slow intensity fluctuations of excitation fields occur. It can also be used effectively in assuring equal operations in a large ensemble of particles. The requirements for the scheme are that a sufficient number of levels are available for implementation, and that energy shifts due to excitation fields (such as AC Stark shifts) can be avoided.

Elimination of AC Stark shifts is not a straightforward task for the scheme presented here since a number of fields with time-dependent amplitudes are used. It can be confirmed from numerical simulations that the operations of the STIRAP gates are not sensitive to one-photon detunings (i.e. detunings for $|i\rangle$–$|u\rangle$ where $i = 0, 1$ and 2) but to every two-photon detuning, and hence all relative shifts between two of $|0\rangle$, $|1\rangle$ and $|2\rangle$ should be minimized. This might be relatively complicated for $e.g.$ $^{40}$Ca$^+$ since, in addition to adjacent Zeeman components in $S_{1/2}$–$D_{5/2}$, dipole-allowed transitions such as $S_{1/2}$–$P_{1/2}$, $S_{1/2}$–$P_{3/2}$ and $D_{5/2}$–$P_{3/2}$ also give rise to appreciable AC Stark shifts[20].

The scheme demonstrated here realizes single-qubit operations that are in general noncommutable to each other by using adiabatic manipulation of dark states.

These amount to implementations of noncommutable (non-Abelian) holonomies, which can be a building block of HQC by Zanardi *et al.*[2] and leads to application in other fields including neutral-atom systems [21].

[1] J. P. Home *et al.*, Science **325**, 1227 (2009); D. Hanneke *et al.*, Nature Phys. **6**, 13 (2010); B. P. Lanyon *et al.*, Science **333**, 57 (2011); T. Monz *et al.*, Phys. Rev. Lett. **106**, 130506 (2011).

[2] P. Zanardi and M. Rasetti, Phys. Lett. A **264**, 94 (1999).

[3] E. Sjöqvist, Physics **1**, 35 (2008).

[4] J. A. Jones *et al.*, Nature **403**, 869 (2000).

[5] D. Leibfried *et al.*, Nature **422**, 412 (2003).

[6] M. Z. Tian, Z. W. Barber, J. A. Fischer, and W. R. Babbitt, Phys. Rev. A **69**, 050301 (2004).

[7] H. Imai and A. Morinaga, Phys. Rev. A **78**, 010302 (2008).

[8] J. Benhelm *et al.*, Nature Phys. **4**, 463 (2008).

[9] A. Barenco *et al.*, Phys. Rev. A **52**, 3457 (1995).

[10] K. Mølmer and A. Sørensen, Phys. Rev. Lett. **82**, 1835 (1999).

[11] C. A. Sackett *et al.*, Nature **404**, 256 (2000).

[12] L. M. Duan *et al.*, Science **292**, 1695 (2001).

[13] Z. Kis and F.Renzoni, Phys. Rev. A **65**, 032318 (2002).

[14] D. Møller, L. B. Madsen, and K. Mølmer, Phys. Rev. A **75**, 062302 (2007).

[15] R. Unanyan *et al.*, Opt. Commun. **155**, 144 (1998).

[16] A. Messiah, *Quantum mechanics* (North-Holland, Amsterdam, 1961), Vol. 2.

[17] K. Toyoda *et al.*, Phys. Rev. A **83**, 022315 (2011).

[18] T. Ohno *et al.*, Jpn. J. Appl. Phys. **50**, 122801 (2011).

[19] H. Dehmelt, Bull. Am. Phys. Soc. **20**, 60 (1975).

[20] H. Häffner *et al.*, Phys. Rev. Lett. **90**, 143602 (2003).

[21] K. Osterloh, M. Baig, L. Santos, P. Zoller, and M. Lewenstein, Phys. Rev. Lett. **95**, 010403 (2005); J. Ruseckas, G. Juzeliunas, P. Ohberg, and M. Fleischhauer, Phys. Rev. Lett. **95**, 010404 (2005); J. Dalibard, F. Gerbier, G. Juzeliunas, and P. Ohberg, Rev. Mod. Phys. **83**, 1523 (2011).
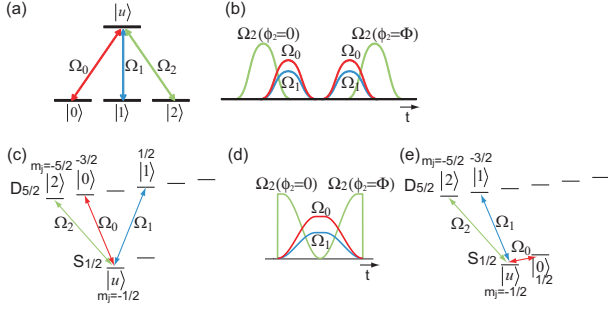
FIG. 1: (Color online) (a) Level scheme of a four-level system used to implement holonomic single-qubit operations. (b) Pulse sequence for holonomic single-qubit operations. (c) Level scheme used for $^{40}$Ca$^+$ in the experiment. (d) Experimentally used pulse sequence. (e) Level scheme that implements another four-level system containing one RF and two optical transitions, with qubit levels $|0\rangle$, $|1\rangle$ separated by an optical frequency.
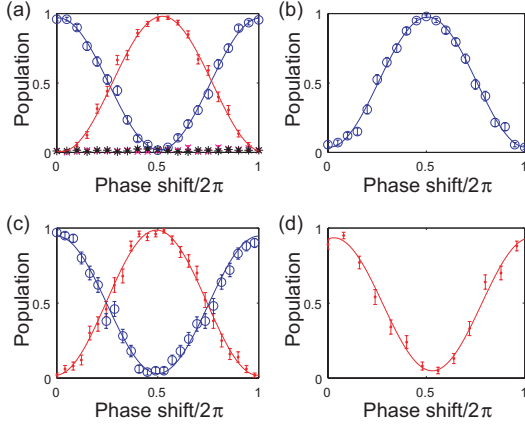


FIG. 2: (Color online) Results of single-qubit rotations ($X$- and $Z$-rotations). Variations of population are plotted against the phase shift in the middle of the gate pulse. The number of experiments per data points is 200 for experiments using three optical transitions [(a) and (b)] and 100 for those using one RF and two optical transitions [(c) and (d)]. The error bars represent errors in projection measurements, which are derived as standard deviations in binomial distributions with numbers of samples as just given. (a) Results for $X$-rotations using three optical transitions. Blue hollow circles, red filled circles, magenta crosses and black asterisks represent the populations in $|0\rangle$, $|1\rangle$, $|2\rangle$ and $|u\rangle$, respectively. (b) Results for $Z$-rotations using three optical transitions. The population in $|0\rangle$ is plotted. (c) Results for $X$-rotations using one RF and two optical transitions. Red filled circles (blue hollow circles) represent the populations in $|1\rangle$ and $|2\rangle$ when $|0\rangle$ ($|1\rangle$) is initially prepared. (d) Results for $Z$-rotations using one RF and two optical transitions. The population in $|1\rangle$ and $|2\rangle$ is plotted.
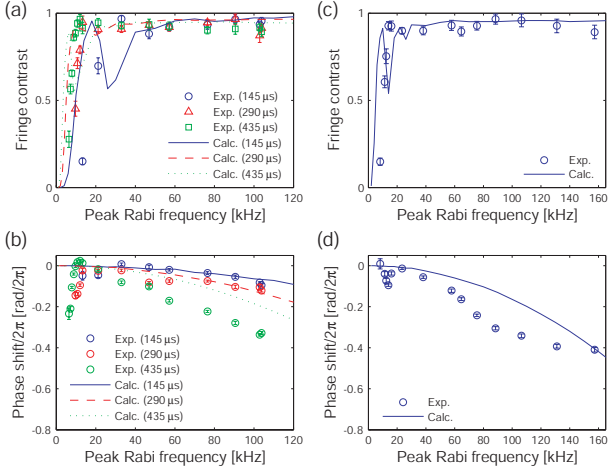
FIG. 3: (Color online) Demonstration of the robustness of single-qubit operations. Each point represent the fringe contrast and shift of the population oscillation obtained by varying the rotation angle of a certain gate operation. Here the rotation angle is varied from 0 to $2\pi$ in 17 steps, and the number of experiments per angle step is 50. The errors in the population measurements are estimated in the same way as in Fig. 2, and the fringe contrasts and shifts are obtained through weighted fits considering those errors. The error bars in the figure represents errors in the fitted parameters. $\alpha = 0.55$ is used here. (a)Fringe contrasts and (b) shifts for $X$-rotations as the peak Rabi frequencies are varied. Here the ratios of the peak values are fixed. The horizontal axis represents the peak value of $\Omega_2$, and the blue circles, red triangles and green squares represent the results for pulse durations of 145, 290 and 435 $\mu$s, respectively. Numerically calculated results for pulse durations of 145, 290 and 435 $\mu$s are also plotted as blue solid curves, red dashed curves and green dotted curves, respectively. (c) Fringe contrasts and (d) shifts for $Z$-rotations as the peak Rabi frequencies are varied. The ratios of the peak values are fixed. Numerically calculated results are also plotted as a blue solid curve.